A Hybrid-Density Functional Theory Study of Intrinsic Point Defects in MX_2 (M = Mo, W; X = S, Se) Monolayers

Alaa Akkoush,* Yair Litman, and Mariana Rossi*

Defects can strongly influence the electronic, optical, and mechanical properties of 2D materials, making defect stability under different thermodynamic conditions crucial for material–property engineering. Herein, an account of the structural and electronic characteristics of point defects in monolayer transition metal dichalcogenides MX_2 with M = Mo/W and X = S/Se is investigated through density functional theory using the hybrid HSE06 exchange–correlation functional including many-body dispersion corrections. For the simulation of charged defects, a charge compensation scheme based on the virtual crystal approximation (VCA) is employed. The study relates the stability and the electronic structure of charged vacancy defects in monolayer MoS_2 to an explicit calculation of the S monovacancy in MoS_2 supported on Au(111), and finds convincing indication that the defect is negatively charged. Moreover, it is shown that the finite-temperature vibrational contributions to the free energy of defect formation can change the stability transition between adatoms and monovacancies by 300–400 K. Finally, defect vibrational properties are probed by calculating a tip-enhanced Raman scattering image of a vibrational mode of a MoS_2 cluster with and without an S monovacancy.

1. Introduction

Transition metal dichalcogenide (TMDC) materials are the subject of intense research, motivated by the possibility of realizing and exploiting novel material properties with ease. The chemical composition of these materials is MX_2, where M is a transition metal atom from groups IV-X and X are chalcogenide atoms, which are stacked in X–M–X layered structures in the bulk. The layers are bonded by van der Waals interactions and thus easy to exfoliate or grow as single layers. Semiconductor TMDCs with M = Mo, W and X = S, Se exhibit an indirect bandgap that becomes a direct gap at the Brillouin-zone K point in the monolayer limit, as a consequence of quantum confinement.[1,2] In addition, because of the moderate and quasi-2D electronic screening,[3] these materials also present a high exciton binding energy, resulting in stable excitons at elevated temperatures.[4] These characteristics make these materials highly desirable for optoelectronic and many other applications.[5–8]

Defects such as vacancies, intercalation, and substitutional atoms are inevitably present in TMDC monolayers generated by any experimental technique[9,10] and often also created on purpose. Because it is easy to reach a high concentration of defects in these materials and therefore induce significant changes in (opto)electronic properties,[11–13] the literature has given much attention to the characterization of defects in TMDCs.[14–20] The presence of defects can be detrimental or advantageous, depending on the targeted property. To cite a few examples, defect-bound neutral excitons have been shown to form characteristic features in the photoluminescence spectra of monolayer TMDCs[21] and chalcogen vacancies have been connected to the dynamics of grain boundaries that strongly impact electronic transport properties.[22] The presence of defects can also serve as an anchor to dock organic molecules and build robust organic–inorganic interfaces with 2D materials that allow, for example, the fabrication of field-effect transistor biosensors.[9,23]

Numerous theoretical studies, which we discuss throughout this article, were carried out on these systems. These studies have provided a comprehensive understanding of the stability of intrinsic point defects. Nevertheless, a few important aspects still deserve a closer examination, such as the vibrational contributions to the thermodynamic stability at elevated temperatures with accurate density functional theory (DFT) calculations, the impact of including many-body van der Waals corrections in calculations, the charge state of defects on metal-supported TMDCs, and the local vibrational properties related to the presence of defects.

A. Akkoush, M. Rossi
Fritz Haber Institute of the Max Planck Society
Faradayweg 4–6, 14195 Berlin, Germany
E-mail: akkoush@fhi-berlin.mpg.de; alaa.akkoush@gmail.com; mariana.rossi@mpsd.mpg.de

A. Akkoush, M. Rossi
Max Planck Institute for the Structure and Dynamics of Matter
Luruper Chaussee 149, 22761 Hamburg, Germany

Y. Litman
Yusuf Hamied Department of Chemistry
University of Cambridge
Lensfield Road, Cambridge CB2 1EW, UK

The ORCID identification number(s) for the author(s) of this article can be found under https://doi.org/10.1002/pssa.202300180.

In this article, we report our results regarding the thermodynamic stability of neutral and charged point defects in monolayer MoS_2, $MoSe_2$, WS_2, and WSe_2 utilizing DFT with a hybrid exchange–correlation functional (HSE06)[24] and employing many-body van der Waals corrections (MBD).[25] We pay particular attention to the vibrational enthalpic and entropic contributions to the defect formation energies at elevated temperatures. For charged defects, we adopt the virtual crystal approximation (VCA)[26,27] scheme to obtain an effective charge compensation in periodic calculations. We present results with this technique, together with an analysis of the electronic structure of the charged systems and a discussion about the charge state of an S vacancy of monolayer MoS_2 adsorbed on Au(111). Finally, we report an analysis of the variations in space-resolved Raman scattering signals due to an S monovacancy in a MoS_2 cluster.

2. Results and Discussion

2.1. Formation Energies of Point Defects

We have considered monolayer 1H MX_2, where M stands for Mo, W and X for S, Se. We have investigated the following common intrinsic point defects: X monovacancy defects (VX); M monovacancy defects (VM); "up and down" divacancies (VX2), where we removed two X atoms from the top and bottom layers lying on coincident lattice sites; neighboring divacancies (VX22), in which two nearest-neighbor X atoms at the same layer are removed; and X adatoms (AddX), where one X atom is added on top of a host
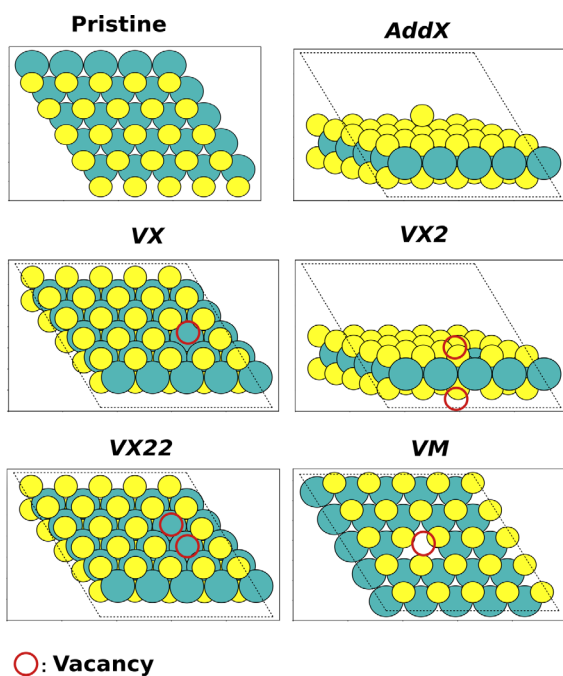

Figure 1. The geometries of the point defects under study for MX_2, M = W, Mo and X = Se, S. AddX stands for an X adatom, VX/M stands for X/M monovacancy, VX2 stands for X divacancies at the top and bottom coincident lattice sites, and VX22 stands for X divacancies at neighboring sites. We use these labels to refer to the defects throughout this article. M atoms are green and X atoms are yellow.

X atom. These defects are shown in **Figure 1**. For VX, we have also considered charged defects (+1/−1), as discussed in Section 4.4.2.

We calculated the formation energies E_f^d as in Equation (1) for the various point defects shown in Figure 1, as a function of the possible chemical potentials of X = S, Se. The chemical potentials μ_X were varied between poor and rich X conditions, as defined in Section 4. We were interested in analyzing the differences between an evaluation of such energies with the PBE + MBD and the HSE06 + MBD functionals. These results are shown in **Figure 2**, where we referenced $\Delta\mu_X = 0$ to the X-rich conditions. Our results agree with results reported previously in the literature, such as the ones presented in refs. [16,17,28,29]. When improving the description of the electronic structure of these systems, by going from the PBE to the HSE06 functional, the energetic hierarchy among the various defects remains the same for all systems. However, the points at which stability transitions are observed change. In particular, for WSe_2 with HSE06 there is no stability transition between AddX and VX toward the poor X conditions. We observe the largest differences in formation energies between PBE and HSE06 for the transition metal vacancies VM in all cases. This observation could be correlated with differences between PBE and HSE06 predicted bandgaps. Among all defects studied here, the PBE bandgaps of VM lie in the range of 0.1–0.4 eV, being the smallest bandgaps of all defects, as shown in Table S3–S7, Supporting Information.

The formation energies of AddX and VX are always lower than those of the other vacancies in either X-rich or M-rich conditions. AddX appears as the most stable out of all neutral point defects at X-rich conditions and over the majority of the possible energy range of μ_X (as also reported in refs. [17,30,31]). As one could expect, the formation energy of divacancies amounts to around twice the formation energy of the monovacancy. However, the results show that for X = Se, the up and down divacancies VSe2 are more favorable than neighboring VSe22 in all investigated TMDCs (in agreement with ref. [29]).

The results presented in this section corroborate most previous work that have investigated defect formation energies in TMDCs.[16,17,29,32,31] The consideration of many-body van der Waals effects, absent in most publications in the literature, shows little impact on these ground-state formation energies.

2.2. Impact of Temperature and Pressure on Defect Stability

In order to obtain more insights on the defect stability at various thermodynamic conditions, we analyzed the connection of the transition points between the most stable defects with temperature and partial pressure. In the calculations, we considered the main contribution of pressure to stem from the chemical potential term, and disregarded lattice expansion effects on the TMDCs. We assume that volume-change contributions will largely cancel when evaluating formation energies. As shown in ref. [16], however, at temperatures above 1000 K, the volume changes can amount to differences of ≈0.2 eV in the formation energies.

We show in **Figure 3** the stability transition lines between VX and AddX for ML MoS_2, $MoSe_2$, and WS_2 as a function of temperature and partial S/Se pressure. We calculate these transitions with and without the temperature-dependent vibrational contributions from the term labeled $\Delta F(T)$ in Equation (11). We do not
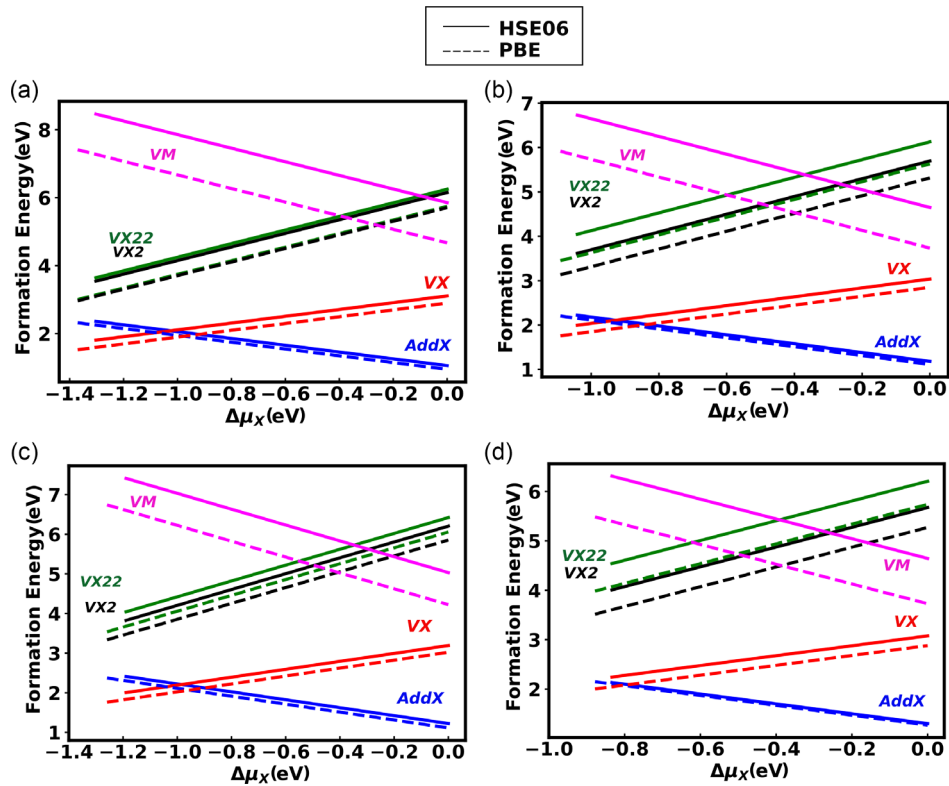
Figure 2. Variation of formation energy (eV) of point defects as a function of X chemical potential, referenced with respect to the X-rich conditions. Dashed lines represent formation energies computed with PBE + MBD and solid lines with HSE06 + MBD for a) MoS_2, b) $MoSe_2$, c) WS_2, and d) WSe_2.
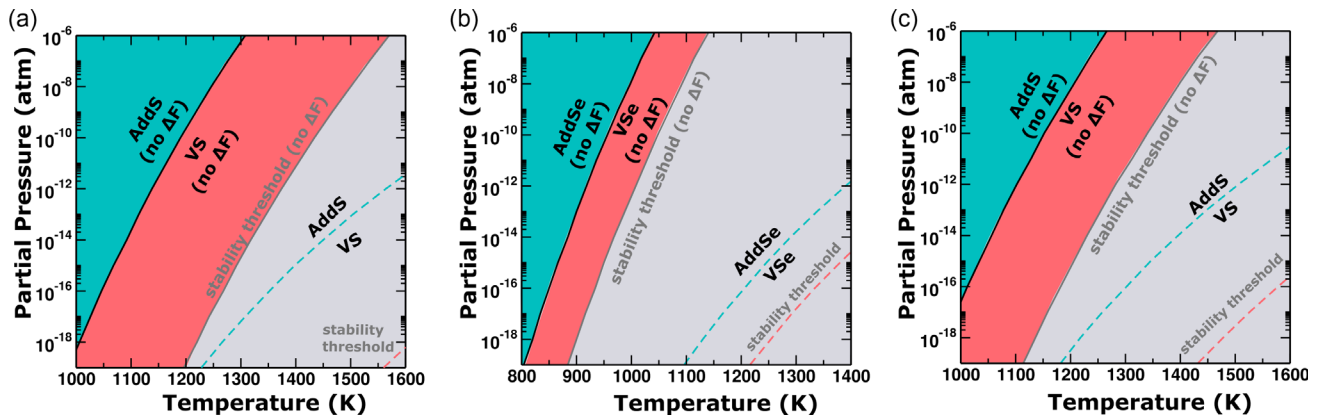

Figure 3. Stability transitions between AddX and VX at different temperatures and partial pressures of S or Se (Equation (12)) for a) MoS_2, b) $MoSe_2$, and c) WS_2. The full lines represent the boundaries without the vibrational contribution $\Delta F(T)$ and the dashed lines the full formation energy as in Equation (11).

show WSe_2 because no stability transition within the boundaries of the chemical potential are predicted for the HSE06 + MBD formation energies. We note that considering a different allotrope for the Se reference could slightly change this picture.

We first focus on the stability ranges obtained without considering the term labeled $\Delta F(T)$ in Equation (11). This term is the vibrational Helmholtz free energy difference between the pristine system and the system containing the defect. This term is commonly disregarded in these calculations because it tends

to be small in more traditional systems.[33] This means that the p, T dependence of the data represented in Figure 3 by the full lines stems only from the terms in Eq. 12. The data presented in Figure 2 are therefore equivalent to the one presented in Figure 3. However, Figure 3 makes it clear that while for $MoSe_2$ the vacancy is stable at much lower temperatures with respect to the S containing systems, its stability range is narrower because the monolayer material ceases to be stable also at lower temperatures when considering equilibrium with the these

ADVANCED
SCIENCE NEWS

www.advancedsciencenews.com

physica
status
solidi
a

www.pss-a.com

reservoirs. The stability range of VS on MoS_2 and WS_2 is larger but starts at higher temperatures. VS in MoS_2 shows the largest temperature stability range.

We then quantify the impact of $\Delta F(T)$ in the defect formation energy of all materials shown in Figure 3. We observe that including ΔF (dashed lines in Figure 3) would increase the transition temperature between AddX and VX by 300–400 K, for a given partial pressure. We note that in this case the boundaries of the chemical potential at each temperature are also different because the temperature-dependent vibrational contributions to the bulk and the monolayer must be included in Equation (9). This naturally raises the question of why AddX defects are rarely observed in experiments. As AddX defects are the most stable over a wide range of temperatures and partial pressures, it may be easy to reach larger concentrations of these defects, making it likely that two or more such defects come into contact. For MoS_2 it was shown by Komsa and Krasheninnikov[16] that as two AddS defects meet, it becomes favorable to desorb a S_2 molecule, especially at elevated temperatures. The increased stability of VX at higher temperatures allied to the proposition that multiple AddX defects can easily desorb could explain why AddS and AddSe are rarely observed in chemical vapor deposition (CVD)-grown TMDCs, while monovacancies are very often observed.[34–36]

Therefore, we note that for monolayer TMDCs the vibrational contributions play an important role on the point defect stability. We note that probably this effect is more pronounced due to the high-temperature regimes relevant for these systems. At lower temperatures, for example, below 600 K, the effect of including or ignoring ΔF is much less pronounced, as exemplified in Figure S4, Supporting Information.

2.3. Charged Monovacancies

Next, we proceeded to analyze defects that carry an electric charge. Because we have established that the qualitative hierarchy of defect formation energies is similar for all systems, we focus on the case of MoS_2. In addition, we consider only charged S monovacancies (VS) because they are the most abundant charged defects appearing in experimentally relevant conditions.[37,38] In **Figure 4** we show the formation energies as calculated from Equation (2), with varying E_f and for $\mu_S = 0.0$ eV
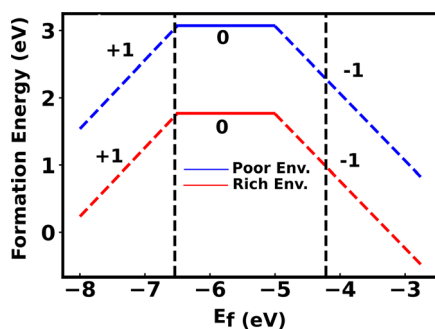

Figure 4. Formation energy of neutral and charged ($q = +1, 0, -1$) VS in MoS_2 computed with HSE06 + MBD as a function of Fermi level (E_f) in the S-rich (blue) and S-poor (red) conditions. E_f is referenced to the vacuum level. The dashed lines mark the position of the VBM and the CBM of the pristine MoS_2 ML.

(rich S) and $\mu_S = -1.3$ eV (poor S). We show the data obtained with the charge compensation scheme discussed in Section 4 including corrections to obtain the dilute limit. We note that we performed spin-polarized calculations for the charged defects.

In the pristine MoS_2 ML, the computed E_{VBM} is at -6.54 eV and the E_{CBM} is at -4.22 eV (HSE06) with respect to the vacuum level. These energies are marked in Figure 4. We observe that the positive charge state is predicted to be stable very close to the VBM (similar to what was reported in refs. [15,16]), while the $(0/-1)$ charge transition level is well within the gap and the negatively charged vacancy is stable for E_f values greater than 1.5 eV above the VBM.

In **Figure 5** we compare the electronic density of states (including spin–orbit coupling) of the pristine MoS_2 monolayer, the neutral S vacancy, and the charged S vacancies. In all cases, we obtain integer occupation of all energy levels and the ground state of the charged defects is a doublet. The results shown for the neutral VS confirm DFT results from other authors,[15,39,40] showing a shallow occupied defect state close to the VBM, and two spin-degenerate unoccupied states in the gap. All these states are of d character and arise from the dangling bonds of the Mo $4d$ orbitals and the reduced Mo $4d$ and S $3p$ orbital hybridization. The splitting between the two unoccupied states is due to spin–orbit coupling. A visualization of the state-resolved electronic density of these defect states is shown in Figure S5, Supporting Information.

We start by discussing the positively charged VS. An unoccupied state with the same character as the shallow occupied state in the neutral VS appears in the gap. This confirms that the orbital that lost one electron is the localized vacancy state, remembering that one spin-channel remains occupied. The vacancy states deep in the gap show a much larger splitting and are not anymore spin-degenerate. As shown in Figure S5, Supporting Information, the states are now grouped by their dominant spin character, and the splitting could be attributed to an exchange interaction with the singly occupied state that lost one electron. We do not observe a structural symmetry breaking around the vacancy. The three Mo atoms around the vacancy form an equilateral triangle with a side length of 3.13 Å. This is consistent with the fact that all vacancy states show the same character as they had in the neutral case, as shown in Figure S5, Supporting Information. It is worth noting that this geometry is, nevertheless, different from the neutral vacancy, where the equilateral triangle defined by the three neighboring Mo atoms surrounding the vacancy has a side of length 3.04 Å in our calculations.

The negatively charged S monovacancy causes a pronounced symmetry breaking on the electronic and atomic structure, characteristic of the Jahn–Teller effect, as discussed previously in ref. [15]. Whereas in ref. [15] the authors employed GGA and metaGGA functionals, we here corroborate the results with HSE06 and the inclusion of many-body vdW corrections. The structural distortion causes the Mo atoms close to the vacancy to form a isosceles triangle where two sides measure 3.04 Å and one side measures 3.16 Å. The occupied shallow defect state in the neutral case loses its spin degeneracy and one spin channel moves in the gap. The four unoccupied defect states from the neutral vacancy present mixed characters, as shown in Figure S5, Supporting Information, and one of them is fully occupied. The other three (unoccupied) states are found very close to the CBM of the bulk material.
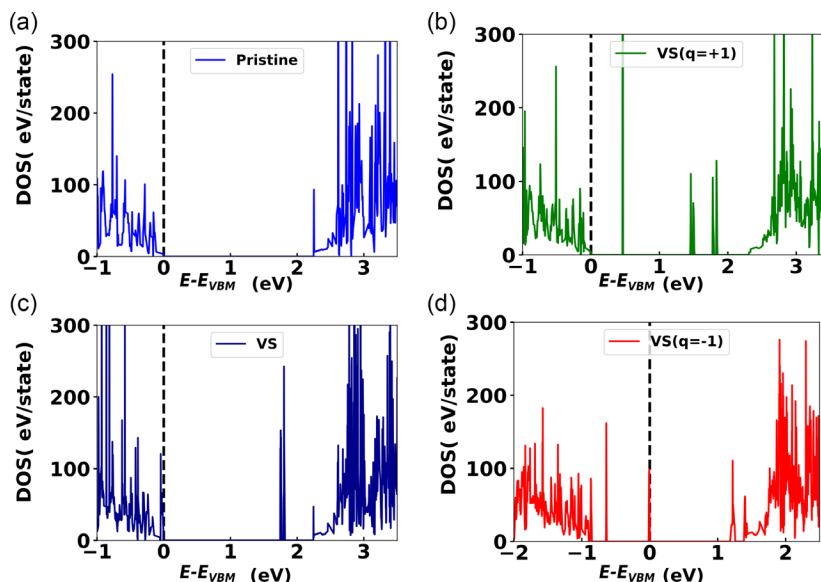
Figure 5. Electronic density of states calculated with the HSE06 functional for a) pristine MoS_2, b) MoS_2 with a positively charged VS ($q = +1$), c) MoS_2 with a neutral VS and d) MoS_2 with a negatively charged VS ($q = -1$).

The calculated stability of the defects and the electronic structure predicted in the calculations are consistent. For completeness, we report the density of states of all neutral point defects under study for MoS_2, $MoSe_2$, WS_2, and WSe_2 computed with HSE06 + MBD including SOC in Figure S6–S9, Supporting Information.

2.4. MoS₂ Monovacancy on Au(111)

In several situations of interest, MoS_2 is supported on an Au(111) substrate.[41,42] The bulk Au Fermi energy is calculated to be -4.95 eV with HSE06 and the basis sets used here, and therefore, it could act as a donating electron reservoir that stabilizes a negatively charged vacancy on MoS_2. Explicitly simulating the MoS_2 monolayer supported by a Au(111) slab requires the use of large supercells in order to minimize the strain induced by the lattice mismatch. We have considered a 8×8 supercell of MoS_2 on a 4-layer 9×9 Au(111) supercell, containing one S vacancy on the vacuum-facing side of MoS_2 (515 atoms), as shown in Figure 4. The MoS_2 ML is stretched by 4.8% in each direction considering HSE06 lattice constants, which induces a small but non-negligible strain on the sheet. However, reducing this number to 1% would require a 12×12 supercell of MoS_2 on a 4-layer 13×13 Au(111) surface, at which point the system becomes too large for obtaining results at this level of theory. We fully relaxed this structure with the HSE06 + MBD (same settings as previously in this article), including spin polarization. We fixed the two bottom Au layers during relaxation. Electronic density of states was calculated with a $4 \times 4 \times 1$ k-point grid for increased accuracy. Fully converging the self-consistent field (SCF) cycle for this structure with HSE06 functional and the FHI-aims code took around 20 h when parallelized over 2304 cores in the MPCDF Raven machine (Intel Xeon IceLake-SP 8360Y). We could not apply spin–orbit coupling corrections to

this structure with this functional due to technical memory issues.

We observe a Moiré pattern formation and a nonuniform distance between the MoS_2 layer and Au(111), as also reported in ref. [42] where they studied similar systems with the PBE functional and dispersion corrections. In this article we are interested in understanding whether this vacancy can be considered negatively charged. We confirm that the structure is magnetic and the states with largest spin asymmetries are those of the d-orbitals of the Mo atoms around the vacancy. We also observe the tell-tale sign of the pronounced structural distortion around the vacancy,
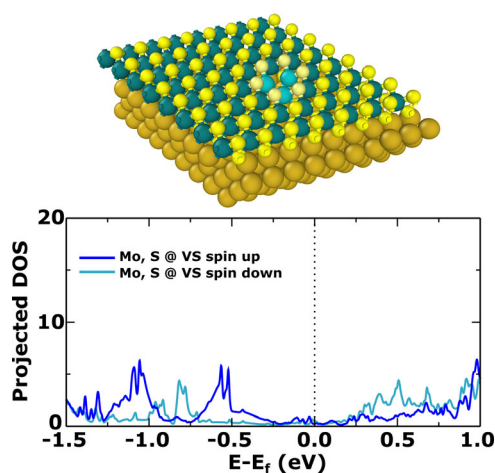

Figure 6. Top: Structure of the 8×8 supercell of MoS_2 on a 4-layer 9×9 Au(111), where we highlight the Mo and S atoms around the vacancy. Bottom: Projected electronic density of states on the highlighted atoms around the vacancy for spin up and spin down channels. Zero represents the Fermi level of the calculation (defined by the states from the Au surface, not shown), above that the states are unoccupied.

with the Mo atoms forming an isosceles triangle with two sides of 3.36 Å and one shorter side of 3.04 Å. Finally, when analyzing the electronic density projected solely on the atoms surrounding the vacancy, as marked and shown in **Figure 6**, we observe occupied states that can be assigned to the vacancy at about −0.5 eV, and we confirmed that they are of Mo d character. These states are also singly occupied, as evidenced by the pronounced spin asymmetry between the channels in this region. All of these observations, connected to the discussions in the previous section, point toward a negatively charged vacancy.

Without further analysis we cannot ascertain the amount of negative charge at the vacancy. Based on the current data we suppose it is at $a-1$ charge state. Previous studies that considered $a-2$ charge state did not find it stable for the monolayer.[16] We note that the structural symmetry breaking is more pronounced and different than the one observed for VS(−1) in free-standing MoS_2 in the previous section, which could be due to the structural strain in this case, or indeed a different charge state. We also note that the metallic substrate is known to induce a considerable gap renormalization on the TMDC monolayers due to screening.[43] A reduction of the bandgap would likely favor the VS(−1) state. Further studies addressing some of these shortcomings and reducing the cost of these large calculations will be the subject of a future work.

2.5. Local Vibrational Fingerprints

Raman spectroscopy is a widely used method to characterize the fundamental vibrational properties of 2D materials.[44] We were interested in exploring the feasibility of using tip-enhanced Raman scattering (TERS) signals to obtain a local description of vibrational properties of the vacancies. The cluster models we use for these calculations do not show the characteristic Raman active E_{2g}^1 (in-plane vibrations) and A_{1g} (out-of-plane vibrations) vibrational modes of monolayer MoS_2[44,45] due to local distortions, but many modes with similar characteristics are present. We show the nonresonant harmonic Raman spectra of the pristine cluster, and the one containing the vacancy in **Figure 7**. The Raman intensities shown in Figure 7 were calculated considering only the square of the variation of α_{zz}
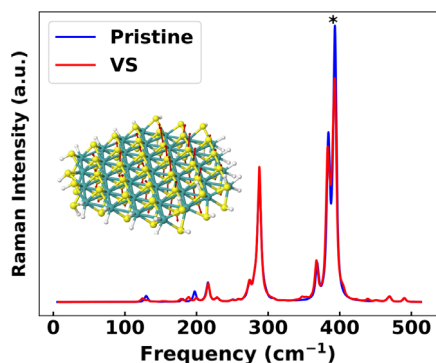

Figure 7. Raman spectra of the MoS_2 cluster with and without the sulfur vacancy. The mode shown in the inset is the one marked with an asterisk for the pristine cluster. The mode resembles the A_{1g} mode of the periodic structure.

component of the polarizability tensor with respect to the normal modes of the system. The cluster was oriented such that the z axis was perpendicular to the surface plane. Because of the presence of the edges, the clusters show many active Raman modes. The most intense peak for both systems, lying at 393 cm^{-1}, corresponds to a mode that resembles the A_{1g} mode in the periodic structure, and this is the mode that we chose to further characterize by means of a simulation of spatially resolved TERS.

We calculated the tip-enhanced Raman intensity according to the methodology proposed in ref. [46], over a region of 9×9 Å^2 covering the defect area. These results are presented in **Figure 8**. We observe that while the Raman spectra of the systems with and without the vacancy shown in Figure 7 are very similar, the TERS signals of the pristine system and the vacancy-containing system are substantially different around the vacancy, despite their very similar frequency and overall character. This result shows the possibility of identifying specific vibrational fingerprints of defects in 2D materials even at low defect concentrations.

We note that our calculations do not include excitonic states, but these could be included, at least approximately, by performing linear-response time-dependent (TD)-DFT calculations with an appropriate functional,[47] instead of density functional perturbation theory calculations within this method. Probably, such a combination would still be considerably more efficient than a full real-time TD-DFT calculation of the TERS signal.

3. Conclusions

We presented a hybrid DFT study of point defects on semiconductor TMDC monolayers MX_2. An analysis of the ground-state formation energy of neutral defects showed that adatom defects are the most stable defects at X-rich conditions and through a wide range of chemical potentials. TMDCs containing X = S show a small range of S monovacancy stability toward S poor conditions, while this range is reduced for TMDCs containing X = Se. A comparison of these formation energies obtained with the PBE + MBD and the HSE06 + MBD functionals shows that only quantitative changes in the energy hierarchy of defect formation energies take place. The largest difference was observed for the Mo and W monovacancies, which could be correlated with the extremely small bandgap predicted by PBE + MBD for these systems. Comparing the results obtained in this study and previous results in the literature that did not employ many-body van der Waals corrections, we also conclude that these have a minor quantitative impact on formation energies. This is not surprising because the main contribution to the defect formation energy in monolayer TMDCs stems from breaking or making covalent bonds. These corrections could have a larger impact in multilayered systems.

Analyzing the transitions between VX and AddX at temperature versus partial pressure diagrams, we concluded that VS is the most stable defect only at very elevated temperatures (>1000 K) for a wide range of partial pressures. VSe is stable at lower temperatures, but its temperature stability range is narrower due to the threshold imposed by the equilibrium with the reservoirs. We also explicitly quantified the effect of vibrational
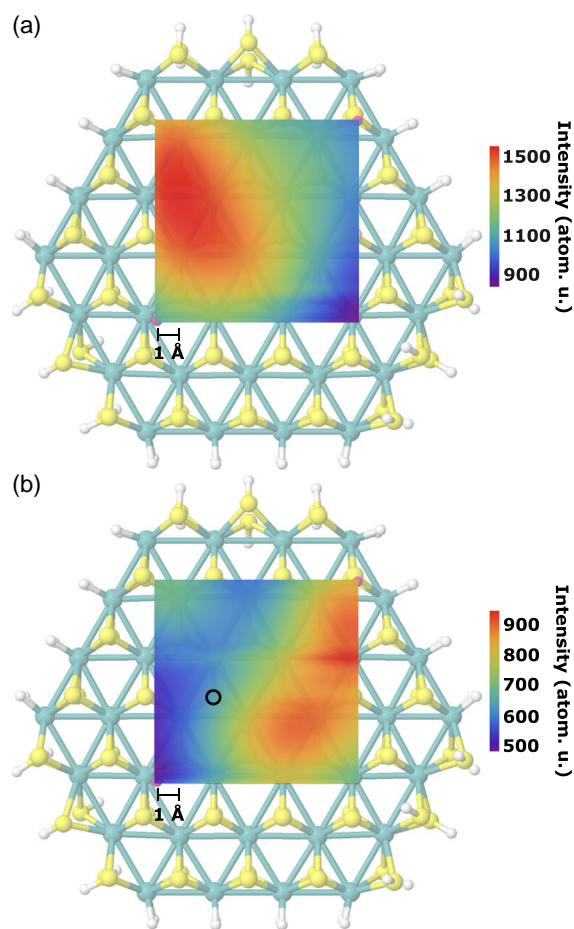
Figure 8. TERS image of the vibrational modes labeled with an asterisk in Figure 7 in the MoS_2 cluster corresponding. a) Pristine system. b) System including the S monovacancy. The position of the S vacancy is marked with a black circle and the pink dots are just visual markers to delimit the image area. Intensities are reported taking into account only the term corresponding to the polarizability variation.

contributions of the TMDC to the formation free energy. We find that these contributions stabilize AddX defects and destabilize VX defects. Disregarding such contributions would lead to a prediction of the stability crossover points between AddX and VX that would be underestimated by 300–400 K in all materials—an effect probably exacerbated by the high temperatures at which this transition occurs. These elevated temperatures are nevertheless relevant for some TMDC growth techniques such as chemical vapor deposition.

For charged defects, we find that the virtual crystal approximation (VCA) in an all-electron electronic structure infrastructure is a simple and powerful technique that allows the simulation of charged defects in these 2D systems within a periodic 3D setup. We combined it with a straightforward extrapolation correction for the remaining lateral interactions between charged defects to reach the dilute limit. With this technique, we could confirm the stability of the negatively charged S vacancy in MoS_2 with a $(0/-1)$ charge transition level within the gap, and characterized the accompanying Jahn–Teller distortion at the electronic and the atomic structure levels. We then analyzed the electronic and atomic structure of the S monovacancy on a MoS_2 monolayer supported on Au(111)

with the HSE06 + MBD functional. This analysis and a comparison to the results of the S monovacancy in the free-standing monolayer led us to conclude that the vacancy is negatively charged in this structure. The VCA scheme can be extended to mimic the charge compensation at the Au substrate instead of within the layer and this is the subject of ongoing work. Many of the techniques discussed here could be used in a high-throughput workflow to augment or complement existing data in databases of defects in 2D materials.[19]

In the future, we plan to conduct a deeper analysis of the specific phonon modes that play a role on the stabilization and destabilization of different defects, and their real-space characteristics. In that respect, the exploratory tip-enhanced Raman scattering calculations presented in this work are very encouraging. We believe that a better characterization of the local Raman signal around defects in 2D materials and the possibility of a direct experiment-theory comparison in real space can give unique insights into the atomic motions that accompany charge localization, exciton trapping, and polaron formation. We consider such insights particularly interesting to guide the chemical design of organic–inorganic interfaces based on 2D materials for optoelectronic and sensor technologies.

4. Computational Section

Basic Parameters: Our calculations have been performed using the FHI-aims[48] program package and periodic boundary conditions. In order to approximate the dilute limit, we aimed at minimizing the interaction between defects in neighboring supercell images. As shown in Figure S1, Supporting Information, the variation of the defect formation energy between a 5×5 supercell and a 7×7 supercell did not exceed 0.03 eV in all studied monolayers. As discussed in the next section, for MoS_2 further corrections to the infinite-size limit brought a further 10 meV correction. We thus chose a 5×5 supercell to perform most calculations in this work and added a vacuum region of around 100 Å to decouple periodic images in the direction perpendicular to the monolayer surfaces. For charged defects we employ further corrections, as explained in section 4.2.

Electronic structure properties and geometry optimizations were obtained with the Perdew, Burke, and Ernzerhof (PBE)[49] and the HSE06 exchange–correlation functional as proposed by Heyd, Scuseria and Ernzerhof[50,51] with 25% exact exchange and the screening parameter $\omega = 0.11$ Bohr^{-1}. Van der Waals (VDW) interactions were accounted for using a many-body dispersion (MBD) model[52] (HSE06 + MBD and PBE + MBD). We performed spin polarized calculations and employed intermediate defaults for basis sets and numerical grid settings in the FHI-aims code.[53] A k-grid of $4 \times 4 \times 1$ was used for geometry optimizations, total energy evaluations and electronic-structure property calculations. We have included the effect of spin–orbit coupling, known to substantially affect the energy bands of TMDCs.[54] We employed a "post-processing" correction, applied only after the electronic ground state density is converged.[55] The HSE06 + MBD optimized (experimental) in-plane lattice constants of MoS_2, $MoSe_2$, WS_2, and WSe_2 primitive cells are 3.14 (3.16[56]), 3.26 (3.30[56]), 3.16 (3.15[57]), and 3.27 (3.28[57]) Å, respectively. To calculate phonons, the PBE + MBD functional in FHI-aims was employed with "tight" computational settings. The same van der Waals corrections as mentioned earlier (PBE + MBD) were applied. These settings allowed for the determination of vibrational contributions to the formation energy of defects.

TERS signals were computed using density functional perturbation theory (DFPT) with the local-density approximation (LDA) functional to compute the density response with respect to a localized electric near-field produced from the response of an Ag tetrahedral tip to an external electric field (**Figure 9**a). Details of the methodology are presented in ref. [46]. Technical problems prevent the near-field response calculation of periodic systems in FHI-aims, thus we employed a cluster approximation. To find a suitable cluster model, we investigated three possible structure forms: hexagonal, rhombic, and triangular (details in Supporting Information), with different types of hydrogen passivation at the edges. We fixed the positions of the Mo atoms at the edges of the clusters at their bulk positions. The choice of the clusters is motivated
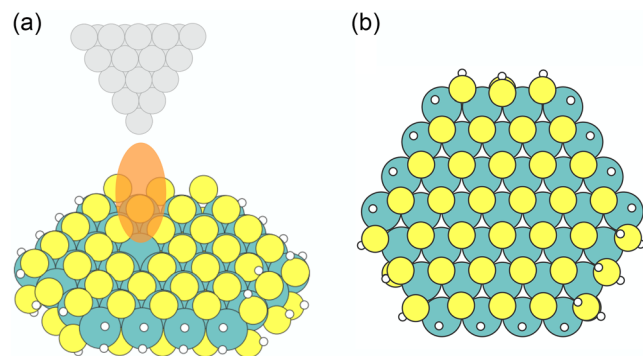
by studies in the literature such as refs. [58,59], where MoS_2 nanoclusters grown on Au(111) were characterized. We selected the cluster with the widest bandgap upon optimization at the PBE + MBD level. This was a hexagonal cluster of 109 atoms of Mo and S with ≈43% S coverage on the edges shown in Figure 7b. Moreover, we confirmed that passivating the cluster edges increased the energy gaps between the highest occupied and the lowest unoccupied molecular orbital due to the removal of the dangling bonds, as previously discussed in a DFT study that explored different sizes of MoS_2 nanoflakes.[60]

Defect Formation Energy: The formation energy of a defect can provide information about their stability under different thermodynamic conditions. We define this formation energy for neutral defects E_f^d as follows

$$E_f^d = E_d(n_i + \Delta n_i) - E_p(n_i) - \sum_i \Delta n_i \mu_i, \qquad (1)$$

where E_d and E_p are the total energy of the defective system and the pristine system, respectively, μ_i is the chemical potential, and Δn_i is the number of atoms of type i that have been added/removed.

For charged defects, the formation energy gains an extra term that accounts for the equilibrium with an electron reservoir (Fermi energy)

$$E_f^d = E_d(n_i + \Delta n_i) - E_p(n_i) - \sum_i \Delta n_i \mu_i + qE_f \qquad (2)$$

where q is the electron charge and E_f is effectively an adjustable parameter that depends on the specific conditions under consideration, and is computed relative to the valence band maximum (VBM) of the defect-free system. We only considered charged defects consisting of X vacancies.

In simulations of charged defects in (free standing) 2D materials using supercells with 3D periodic boundary conditions, we encounter the challenge of performing a charge compensation technique that does not generate spurious interactions. If such interactions do arise, they must be corrected.[61–64] The virtual-crystal approximation (VCA)[26,27,65] has been successful in simulating charged defects at bulk systems and surfaces in the past, and removes the spurious interaction of the charged defect with a homogeneous compensating background charge in surface or 2D-material simulations. In this approximation, when working in an all-electron code like FHI-aims, we modify the nuclear charges ($Z' = Z + \Delta Z$) of certain atoms to modify the number of effective electrons in the system, while the simulation as a whole remains neutral. The nuclear charges are modified as the following

$$\Delta Z = \begin{cases} +\frac{|q|}{N} & \text{for n} - \text{type doping} \\ -\frac{|q|}{N} & \text{for p} - \text{type doping} \end{cases} \qquad (3)$$

where $|q|$ is the absolute value of the desired defect charge of the defect and N is the number of atoms for which the nuclear charge is modified. We note that when doping the system in this manner, the reference energies of the pristine and defected systems appearing in the expression of Equation (2) must be calculated with the same conditions of doping to give a consistent reference. Here, we compensate charges within the TMDC monolayer (ML) itself by modifying the nuclear charge of transition metal atoms through the VCA recipe. We correct the remaining lateral interactions of the charged defects by performing VCA calculations for increasing $L \times L$ supercells with $L = 4, 5, 6, 7, 10$ at the PBE + MBD level, fitting a $E_f^d(\infty) + b/L + c/L^2 + d/L^3$ function to the formation energies.[26] This correction is added to the HSE06 + MBD formation energies calculated with the 5×5 supercell and amounts to about -30 meV for neutral S vacancies and $+200$ meV for the charged S vacancies as shown in Figure S2, Supporting Information.

In all expressions above, the chosen values of the chemical potential μ_i are central to the formation energy analysis. We discuss how to model them in the section below.

Boundaries of Chemical Potentials μ: ML of TMDCs can exist in different conditions of excess of a particular constituent atom. In the calculations, we take these possible environments into account by varying the chemical potential μ_i between two extremes: rich X (poor M) and poor X (rich M) conditions.

For MX_2 MLs, one can consider the thermodynamic equilibrium conditions as

Figure 9. a) Schematic drawing of a TERS setup with an Ag tetrahedral tip over a vacancy defect on an MoS_2 cluster. The orange ellipse denotes the local electric field. b) Geometry of the MoS_2 cluster used in this study for the calculation of the TERS signals. White circles denote hydrogen atoms.

$$\mu_M + 2\mu_X = E_{MX_2}^{ML}$$
$$\mu_X = \frac{1}{2}\left(E_{MX_2}^{ML} - \mu_M\right) \tag{4}$$

where $E_{MX_2}^{ML}$ refers to the total energy of the primitive unit cell. The lower bound of μ_X takes place for M-rich conditions, here modeled by the chemical potential (atomization energy) of M in a bulk BCC structure $\mu_M = \mu_M^{Bulk}$. With that we obtain

$$\mu_X^{min} = \frac{1}{2}\left(E_{MX_2}^{ML} - \mu_M^{Bulk}\right) \tag{5}$$

The upper bound of μ_X (X-rich environment) is taken as the chemical potential of X in an 8-membered homoatomic ring molecule. This is a common reference in the literature.[66,67] The S_8 ring is a predominant S allotrope in the solid and gas phase,[68] while Se_8 is one of three predominately reported Se allotropes in the literature.[69,70]

Therefore

$$\mu_X^{max} = \frac{1}{8}E_{S_8/Se_8} \tag{6}$$

These considerations lead us to

$$\mu_M^{min} = \left(E_{MX_2}^{ML} - 2\mu_X\right) \tag{7}$$

We note that the expressions above automatically determine the boundaries of μ_M. The final boundaries of chemical potentials that we consider are

$$E_{MX_2}^{ML} - 2(E_{S_8/Se_8}/8) \leq \mu_M \leq \mu_M^{Bulk} \tag{8}$$

and

$$\frac{1}{2}\left(E_{MX_2}^{ML} - \mu_M^{Bulk}\right) \leq \mu_X \leq E_{S_8/Se_8}/8 \tag{9}$$

The ranges of chemical potentials ($\mu_X - \mu_X^{max}$) that we have considered for each system are shown in **Table 1**.

Temperature and Pressure Contributions to Formation Energy: In the following, we consider the temperature and partial pressure contributions on the defect formation energies. We consider the Gibbs energy of formation as $G(p,T) = F(V,T) + pV = E - TS + pV$, where F is the Helmholtz free energy, V is the total volume of the system, p stands for pressure, T is the temperature, and S is the entropy. The free energy of defect formation (here considering the case of neutral defects) is given by[61,71]

$$G_f^d(p,T) = G_d(p,T) - G_p(p,T) - \sum_i \Delta n_i \mu_i(p,T) \tag{10}$$

We consider harmonic vibrational contributions to the Helmholtz vibrational free energy $F(T)$, and a fixed volume. For the reference molecules (chemical potential) we take all vibrational frequencies ω_i and for the periodic systems we consider those at the Γ point of the Brillouin zone of the system supercell. Separating this term explicitly in Equation (10) we obtain

$$G_f^d(p,T) = \Delta E + \Delta F(T) - \sum_i \Delta n_i \mu_i(p,T) \tag{11}$$

Table 1. Lower boundaries of $\frac{1}{2}\Delta\mu_M^{min} = \Delta\mu_X^{min} = \frac{1}{2}(E_{MX_2}^{ML} - \mu_M^{Bulk}) - E_{X_8}/8$ for the TMDCs under study using HSE06 + MBD (PBE + MBD). Values are in eV.

	MoS$_2$	MoSe$_2$	WS$_2$	WSe$_2$
$\Delta\mu_X^{min}$	−1.30 (−1.37)	−1.04 (−1.09)	−1.19 (−1.26)	−0.83 (−0.88)

where ΔE is the difference between defect and the pristine ground state total energy and $\Delta F(T)$ is the difference between the respective Helmholtz free energies. For the chemical potential $\mu_i(T,p)$, we can approximate the partition functions of the rotational, translational and vibrational degrees of freedom of the reference molecular reservoir.[72] This leads to the previously reported expressions[61,71]

$$\mu(p,T) = \frac{1}{N_{at}}\left\{-kT\ln\left[\left(\frac{2\pi M}{h^2}\right)^{\frac{3}{2}}\frac{(kT)^{\frac{5}{2}}}{p_0}\right] - kT\ln\left(\frac{\pi^{\frac{1}{2}}}{\sigma}\right)\right.$$
$$- kT\ln\left[\left(\frac{8\pi kT}{h^2}\right)^{\frac{3}{2}}I_A^{\frac{1}{2}}I_B^{\frac{1}{2}}I_C^{\frac{1}{2}}\right] + kT\sum_i\ln\left[1 - \exp\left(-\frac{\hbar\omega_i}{kT}\right)\right]$$
$$\left. + kT\ln\frac{p}{p_0} + E_{ref} + \sum_i\frac{\hbar\omega_i}{2}\right\} \tag{12}$$

where N_{at} is the number of atoms in the molecule or unit cell, M is the total mass of the molecule, ω_i are the harmonic vibrational frequencies, p is the partial pressure of the species for which the chemical potential is being calculated, σ is a molecule-dependent symmetry factor, and I are the moments of inertia along the principle axis of rotation of the molecule. The rotational and translational terms are absent for solid-state references. We take $p_0 = 1$ atm and E_{ref} as the atomization energy of the chemical species under consideration, for the given standard reference. For S and Se our standard references were the S_8 and Se_8 molecules in the gas phase and for Mo and W, the BCC bulk structure. We note that other gas-phase allotropes of S and Se are more stable at elevated temperatures.[68]

Supporting Information

Supporting Information is available from the Wiley Online Library or from the author.

Conflict of Interest

The authors declare no conflict of interest.

Data Availability Statement

The data showcased in this paper can be accessed in the NOMAD Lab database under the DOI address https://doi.org/10.17172/NOMAD/2023.04.29-1.

[1] K. F. Mak, C. Lee, J. Hone, J. Shan, T. F. Heinz, *Phys. Rev. Lett.* **2010**, *105*, 136805.

[2] A. Splendiani, L. Sun, Y. Zhang, T. Li, J. Kim, C.-Y. Chim, G. Galli, F. Wang, *Nano Lett.* **2010**, *10*, 1271.

[3] K. S. Thygesen, *2D Mater.* **2017**, *4*, 022004.

[4] M. M. Ugeda, A. J. Bradley, S.-F. Shi, F. H. Da Jornada, Y. Zhang, D. Y. Qiu, W. Ruan, S.-K. Mo, Z. Hussain, Z.-X. Shen, F. Wang, S. G. Louie, M. F. Crommie, *Nat. Mater.* **2014**, *13*, 1091.

[5] J. S. Ross, P. Klement, A. M. Jones, N. J. Ghimire, J. Yan, D. Mandrus, T. Taniguchi, K. Watanabe, K. Kitamura, W. Yao, D. H. Cobden, X. Xu, *Nat. Nanotechnol.* **2014**, *9*, 268.

[6] H. Zeng, J. Dai, W. Yao, D. Xiao, X. Cui, *Nat. Nanotechnol.* **2012**, *7*, 490.

[7] Y. Yoon, K. Ganapathi, S. Salahuddin, *Nano Lett.* **2011**, *11*, 3768.

[8] S. Park, H. Wang, T. Schultz, D. Shin, R. Ovsyannikov, M. Zacharias, D. Maksimov, M. Meissner, Y. Hasegawa, T. Yamaguchi, S. Kera, A. Aljarb, M. Hakami, L. Li, V. Tung, P. Amsalem, M. Rossi, N. Koch, *Adv. Mater.* **2021**, *33*, 2008677.

[9] Z. Lin, B. R. Carvalho, E. Kahn, R. Lv, R. Rao, H. Terrones, M. A. Pimenta, M. Terrones, *2D Mater.* **2016**, *3*, 022002.

[10] S. Ding, F. Lin, C. Jin, *Nanotechnology* **2021**, *32*, 255701.

[11] S. Tongay, J. Suh, C. Ataca, W. Fan, A. Luce, J. S. Kang, J. Liu, C. Ko, R. Raghunathanan, J. Zhou, F. Ogletree, J. Li, J. C. Grossman, J. Wu, *Sci. Rep.* **2013**, *3*, 2657.

[12] W. Zhou, X. Zou, S. Najmaei, Z. Liu, Y. Shi, J. Kong, J. Lou, P. M. Ajayan, B. I. Yakobson, J.-C. Idrobo, *Nano Lett.* **2013**, *13*, 2615.

[13] A. McCreary, A. Berkdemir, J. Wang, M. A. Nguyen, A. L. Elías, N. Perea-López, K. Fujisawa, B. Kabius, V. Carozo, D. A. Cullen, T. E. Mallouk, J. Zhu, M. Terrones, *J. Mater. Res.* **2016**, *31*, 931.

[14] Q. Liang, Q. Zhang, X. Zhao, M. Liu, A. T. S. Wee, *ACS Nano* **2021**, *15*, 2165.

[15] A. M. Z. Tan, C. Freysoldt, R. G. Hennig, *Phys. Rev. Mater.* **2020**, *4*, 064004.

[16] H.-P. Komsa, A. V. Krasheninnikov, *Phys. Rev. B* **2015**, *91*, 125304.

[17] K. C. Santosh, R. C. Longo, R. Addou, R. M. Wallace, K. Cho, *Nanotechnology* **2014**, *25*, 375703.

[18] Y.-C. Lin, S. Li, H.-P. Komsa, L.-J. Chang, A. V. Krasheninnikov, G. Eda, K. Suenaga, *Adv. Funct. Mater.* **2018**, *28*, 1704210.

[19] F. Bertoldo, S. Ali, S. Manti, K. S. Thygesen, *npj Comput. Mater.* **2022**, *8*, 56.

[20] C. Murray, C. van Efferen, W. Jolie, J. A. Fischer, J. Hall, A. Rosch, A. V. Krasheninnikov, H.-P. Komsa, T. Michely, *ACS Nano* **2020**, *14*, 9176.

[21] P. K. Chow, R. B. Jacobs-Gedrim, J. Gao, T.-M. Lu, B. Yu, H. Terrones, N. Koratkar, *ACS Nano* **2015**, *9*, 1520.

[22] J. Lin, S. T. Pantelides, W. Zhou, *ACS Nano* **2015**, *9*, 5189.

[23] P. Fathi-Hafshejani, N. Azam, L. Wang, M. A. Kuroda, M. C. Hamilton, S. Hasim, M. Mahjouri-Samani, *ACS Nano* **2021**, *15*, 11461.

[24] A. V. Krukau, O. A. Vydrov, A. F. Izmaylov, G. E. Scuseria, *J. Chem. Phys.* **2006a**, *125*, 224106.

[25] J. Hermann, A. Tkatchenko, *Phys. Rev. Lett.* **2020a**, *124*, 146401.

[26] N. A. Richter, S. Sicolo, S. V. Levchenko, J. Sauer, M. Scheffler, *Phys. Rev. Lett.* **2013**, *111*, 045502.

[27] N. A. Richter, Ph.D. Thesis, Technische Universität Berlin **2014**.

[28] N. Guo, X. Fan, Z. Chen, Z. Luo, Y. Hu, Y. An, D. Yang, S. Ma, *Comput. Mater. Sci.* **2020**, *176*, 109540.

[29] D. Yang, X. Fan, F. Zhang, Y. Hu, Z. Luo, *Nanoscale Res. Lett.* **2019**, *14*, 1.

[30] S. Haldar, H. Vovusha, M. K. Yadav, O. Eriksson, B. Sanyal, *Phys. Rev. B* **2015**, *92*, 235408.

[31] W.-F. Li, C. Fang, M. A. van Huis, *Phys. Rev. B* **2016**, *94*, 195425.

[32] H. Shu, D. Zhou, F. Li, D. Cao, X. Chen, *ACS Appl. Mater. Interfaces* **2017**, *9*, 42688.

[33] J. Rogal, K. Reuter, Experiment, Modeling and Simulation of Gas Surface Interactions for Reactive Flows in Hypersonic Flights, 2–1 – 2–18, **2007**.

[34] X. Ling, Y.-H. Lee, Y. Lin, W. Fang, L. Yu, M. S. Dresselhaus, J. Kong, *Nano Lett.* **2014**, *14*, 464.

[35] X. Wang, Y. Gong, G. Shi, W. L. Chow, K. Keyshar, G. Ye, R. Vajtai, J. Lou, Z. Liu, E. Ringe, B. K. Tay, P. M. Ajayan, *ACS Nano* **2014**, *8*, 5125.

[36] J. Hong, Z. Hu, M. Probert, K. Li, D. Lv, X. Yang, L. Gu, N. Mao, Q. Feng, L. Xie, J. Zhang, D. Wu, Z. Zhang, C. Jin, W. Ji, X. Zhang, J. Yuan, Z. Zhang, *Nat. Commun.* **2015**, *6*, 6293.

[37] P. D. Cunningham, K. M. McCreary, A. T. Hanbicki, M. Currie, B. T. Jonker, L. M. Hayden, *J. Phys. Chem. C* **2016**, *120*, 5819.

[38] H. Nan, Z. Wang, W. Wang, Z. Liang, Y. Lu, Q. Chen, D. He, P. Tan, F. Miao, X. Wang, J. Wang, Z. Ni, *ACS Nano* **2014**, *8*, 5738.

[39] B. Zhao, C. Shang, N. Qi, Z. Chen, Z. Chen, *Appl. Surf. Sci.* **2017**, *412*, 385.

[40] K. Santosh, R. C. Longo, R. Addou, R. M. Wallace, K. Cho, *Nanotechnology* **2014**, *25*, 375703.

[41] N. Krane, C. Lotze, K. J. Franke, *Surf. Sci.* **2018**, *678*, 136.

[42] F. Tumino, C. S. Casari, A. L. Bassi, S. Tosoni, *J. Phys. Chem. C* **2020**, *124*, 12424.

[43] M. H. Naik, M. Jain, *Phys. Rev. Mater.* **2018**, *2*, 084002.

[44] W. M. Parkin, A. Balan, L. Liang, P. M. Das, M. Lamparski, C. H. Naylor, J. A. Rodríguez-Manzo, A. C. Johnson, V. Meunier, M. Drndic, *ACS Nano* **2016**, *10*, 4134.

[45] S. Gupta, A. Johnston, S. Khondaker, *J. Appl. Phys.* **2022**, *131*, 164303.

[46] Y. Litman, F. P. Bonafé, A. Akkoush, H. Appel, M. Rossi, **2022**.

[47] Y.-M. Byun, J. Sun, C. A. Ullrich, *Electron. Struct.* **2020**, *2*, 023002.

[48] V. Blum, R. Gehrke, F. Hanke, P. Havu, V. Havu, X. Ren, K. Reuter, M. Scheffler, *Comput. Phys. Commun.* **2009**, *180*, 2175.

[49] J. P. Perdew, K. Burke, M. Ernzerhof, *Phys. Rev. Lett.* **1996**, *77*, 3865.

[50] J. P. Perdew, M. Ernzerhof, K. Burke, *J. Chem. Phys.* **1996**, *105*, 9982.

[51] A. V. Krukau, O. A. Vydrov, A. F. Izmaylov, G. E. Scuseria, *J. Chem. Phys.* **2006b**, *125*, 224106.

[52] J. Hermann, A. Tkatchenko, *Phys. Rev. Lett.* **2020b**, *124*, 146401.

[53] S. V. Levchenko, X. Ren, J. Wieferink, R. Johanni, P. Rinke, V. Blum, M. Scheffler, *Comput. Phys. Commun.* **2015**, *192*, 60.

[54] Z. Y. Zhu, Y. C. Cheng, U. Schwingenschloegl, *Phys. Rev. B* **2011**, *84*, 153402.

[55] W. P. Huhn, V. Blum, *Phys. Rev. Mater.* **2017**, *1*, 033803.

[56] T. Böker, R. Severin, A. Müller, C. Janowitz, R. Manzke, D. Voß, P. Krüger, A. Mazur, J. Pollmann, *Phys. Rev. B* **2001**, *64*, 235305.

[57] W. J. Schutte, J. L. De Boer, F. Jellinek, *J. Solid State Chem. France* **1987**, *70*, 207.

[58] J. V. Lauritsen, J. Kibsgaard, S. Helveg, H. Topsøe, B. S. Clausen, E. Lægsgaard, F. Besenbacher, *Nat. anotechnol.* **2007**, *2*, 53.

[59] S. S. Grønborg, N. Salazar, A. Bruix, J. Rodríguez-Fernández, S. D. Thomsen, B. Hammer, J. V. Lauritsen, *Nat. Commun.* **2018**, *9*, 2211.

[60] M. Javaid, D. W. Drumm, S. P. Russo, A. D. Greentree, *Sci. Rep.* **2017**, *7*, 1.

[61] C. Freysoldt, B. Grabowski, T. Hickel, J. Neugebauer, G. Kresse, A. Janotti, C. G. Van de Walle, *Rev. Mod. Phys.* **2014**, *86*, 253.

[62] C. Freysoldt, J. Neugebauer, C. G. Van de Walle, *Phys. Rev. Lett.* **2009**, *102*, 016402.

[63] H.-P. Komsa, N. Berseneva, A. V. Krasheninnikov, R. M. Nieminen, *Phys. Rev. X* **2014**, *4*, 031044.

[64] O. T. Hofmann, E. Zojer, L. Hörmann, A. Jeindl, R. J. Maurer, *Phys. Chem. Chem. Phys.* **2021**, *23*, 8132.

[65] L. Bellaiche, D. Vanderbilt, *Phys. Rev. B* **2000**, *61*, 7877.

[66] O. Lehtinen, H.-P. Komsa, A. Pulkin, M. B. Whitwick, M.-W. Chen, T. Lehnert, M. J. Mohn, O. V. Yazyev, A. Kis, U. Kaiser, A. V. Krasheninnikov, *ACS Nano* **2015**, *9*, 3274.

[67] C. Jia, B. Zhou, Q. Song, X. Zhang, Z. Jiang, *RSC Adv.* **2018**, *8*, 18837.

[68] R. Steudel, B. Eckert, *Elemental Sulfur and Sulfur-rich Compounds I* Springer, Berlin, Heidelberg **2003**, pp. 1–80.

[69] I. Haiduc, D. B. Sowerby, *The Chemistry of Inorganic Homo-and Heterocycles*, Vol. *2*, Academic Press, New York **1987**.

[70] F. A. Devillanova, W.-W. Du Mont, *Handbook of Chalcogen Chemistry: New Perspectives in Sulfur, Selenium and Tellurium*, Vol. *1*, Royal Society of Chemistry, Cambridge **2013**.

[71] K. Reuter, C. Stampf, M. Scheffler, *Handbook of Materials Modeling*, Springer, Netherlands **2005**, pp. 149–194.

[72] D. McQuarrie, *Statistical Mechanics*, Sterling Publishing Company **2000**.